Journal of Engineering Mathematics (2005) 53: 239–252
DOI 10.1007/s10665-005-9013-2

The effect of the small-aspect-ratio approximation on canonical electrostatic MEMS models

JOHN A. PELESKO and TOBIN A. DRISCOLL
Department of Mathematical Sciences, University of Delaware, Newark, DE, 19716, USA
(E-mail: {pelesko,driscoll}@math.udel.edu)

Received 29 September 2004; accepted in revised form 29 July 2005

Abstract. The mathematical modeling and analysis of electrostatically actuated micro- and nanoelectromechanical systems (MEMS and NEMS) has typically relied upon simplified electrostatic-field approximations to facilitate the analysis. Usually, the small aspect ratio of typical MEMS and NEMS devices is used to simplify Laplace's equation. Terms small in this aspect ratio are ignored. Unfortunately, such an approximation is not uniformly valid in the spatial variables. Here, this approximation is revisited and a uniformly valid asymptotic theory for a general "drum shaped" electrostatically actuated device is presented. The structure of the solution set for the standard non-uniformly valid theory is reviewed and new numerical results for several domain shapes presented. The effect of retaining typically ignored terms on the solution set of the standard theory is explored.

Key words: continuation method, microelectromechanical systems, MEMS, nanoelectromechanical systems, NEMS, nonlinear elliptic problem

1. Introduction

Micro- and nanoelectromechanical systems (MEMS and NEMS) technology is arguably the hottest topic in engineering today. Four decades of advances in this direction, including the development of planar batch-fabrication methods, the invention of the scanning-tunnelling and atomic-force microscopes, and the discovery of the carbon nanotube, have left us poised for a MEMS and NEMS invasion of every aspect of modern life. Yet much remains to be done. Further advances in MEMS and NEMS design require a deeper understanding of basic phenomena at the micro- and nanoscale.

One topic in need of further research is the use of electrostatic forces to move elastic structures at the micro- and nanoscale. With a few important exceptions, such as electro-spraying technology [1], electrostatics in macro-scale engineering has largely been regarded as a nuisance by the engineering community. The main focus of research in this area has been on ways to minimize electrostatic build-up and prevent accidental and destructive electrostatic discharge. With the advent of MEMS and NEMS, electrostatics has gained a seat at the head of the engineering table. This change in status is due to the science of scale. In the micro- and nanoworld, objects are almost all surface. The mass and inertia of microscale objects are essentially negligible. This implies that inertial forces, such as gravity, are largely irrelevant, while forces dominated by surface interactions, such as electrostatic forces, are pre-eminent.

Researchers have recognized and exploited the importance of electrostatic forces at the micro- and nano-level for more than forty years. A seminal development in this area occurred in 1964 when Nathanson and his co-workers at Westinghouse produced the so-called resonant gate transistor [2]. This was not only the first batch-fabricated MEMS device, but was also the

first electrostatically actuated MEMS device as well. Since then, electrostatics has played an important role in the development of devices such as accelerometers [3], optical switches [4], microgrippers [5], micro force gauges [6], transducers [7], and micropumps [8].

In designing almost any MEMS or NEMS device based on the interaction of electrostatic forces with elastic structures, the MEMS designer will confront the ubiquitous "pull-in" instability. In this instability, when applied voltages are increased beyond a certain critical point there is no longer a steady-state configuration of the device where mechanical members remain separate. This instability severely restricts the stable range of operation of many devices [9], and hence a good deal of the mathematical modeling of electrostatic MEMS and NEMS has focused on understanding and controlling this instability. Almost all modeling in this area builds on the work of Nathanson and his co-workers [2] who, in addition to building the first MEMS device, developed a mathematical model of electrostatic-elastic interaction in MEMS. Their model was a mass-spring model similar to that shown in Figure 1. The mechanical members of the system were treated as two rigid plates. One plate was assumed fixed, the other attached to a linear spring. The spring force was balanced by an electrostatic force caused by the application of a voltage difference between the plates. This simple model allowed Nathanson and his co-workers to predict and begin to characterize the pull-in instability. As might be expected, Nathanson *et al.*, introduced an approximation in order to simplify the electrostatic problem and to allow them to easily calculate the electrostatic force on their plates. Since the mechanical system consisted of parallel plates, and since the aspect ratio of their device was small, they assumed the electric field was that due to two infinite parallel plates. They ignored fringing fields at the edges of the plates.

Most investigators studying electrostatic-elastic interactions in MEMS and NEMS have followed Nathanson's lead and used some sort of small aspect ratio approximation to simplify the electrostatic theory. This approach has been fruitful, leading to such advances as the characterization of the pull-in instability in terms of a fold-bifurcation [9], insight into the interesting nonlinear dynamics of electrostatically actuated beams [10], and the development of new schemes for computing the pull-in voltage for a complicated device design [11]. Unfortunately, when examined critically, the canonical small-aspect ratio approximation used by the MEMS and NEMS communities reveals an obvious weakness. This approximation is really only a leading-order *outer* approximation of an asymptotic theory based on expansion in the small aspect ratio. Fringing fields, unaccounted for in the canonical theory, cause

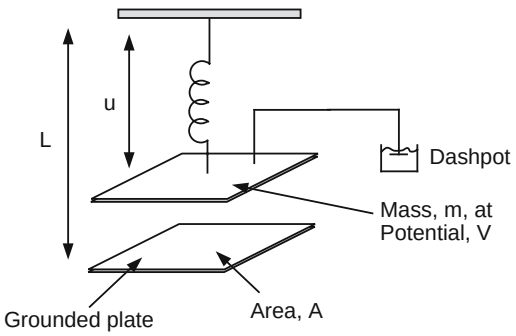

Figure 1. The Nathanson mass-spring model.

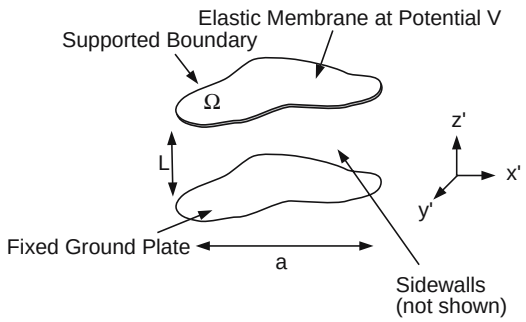

Figure 2. Sketch of our idealized drum shaped system. Note that the sidewalls (not shown), support the membrane and make the structure into a "drum."

an order-one correction in some region close to the boundary. Additionally, since the elastic problem needs as its input the *gradient* of the elastic potential, correction terms arise near internal corners as well.

In this paper we develop a uniformly valid asymptotic approximation to the electrostatic field in a typical MEMS structure. We use this approximation to develop a uniformly valid theory for the electrostatic force on our elastic structure. We then investigate the implications of retaining typically ignored terms on the solutions of the canonical model. We begin in the next section by formulating the governing equations for a drum-shaped MEMS device. To keep matters simple, we take our elastic body to be an elastic membrane. This is valid for some MEMS devices and invalid for others. For examples of each, see [9]. We restrict our attention to those devices well modelled by membrane theory. The field approximations we develop are independent of the elastic theory and may easily be extended to studying beams, plates, or more complicated structures. In Section 3 we develop our asymptotic theory. We use our uniformly valid asymptotic approximation for the electrostatic field to compute a uniform approximation to the electrostatic force on the membrane. We present both the canonical model and the corrected model for our system. In Section 4 we review and extend known results concerning the canonical model. Most importantly, we present the results of a numerical investigation of the canonical model using continuation methods. This allows us to reliably sketch the bifurcation diagram for the standard model and show that the presence of multiple folds occurs for a variety of domain shapes. Previously, this had been suspected, but only verified for disk-shaped domains [12]. In Section 5 we turn to the new corrected model and focus on a disk-shaped domain. We numerically investigate the solution to this corrected model and show that the number of folds in the bifurcation diagram for the model varies with the aspect ratio of the device. Finally, we conclude in Section 6 with a discussion of the implications of these results for MEMS device design and suggestions for future work.

2. Formulation of the model

In this section we present the governing equations for the behavior of our idealized drum-shaped electrostatically actuated MEMS device. Our device consists of a thin elastic membrane suspended above a rigid plate. Both the boundary of the membrane and of the plate are located at $r' = aR(\theta)$, where $R(\theta)$ is a dimensionless 2π-periodic function and a has units of length. The membrane and plate are separated by a gap of height L. The sidewalls supporting the membrane are electrically connected to the plate but are separated from the membrane by a thin insulating layer. In this way, a potential difference is applied between the membrane and the rest of the device. This "drum"-shaped geometry is sketched in Figure 2. With these assumptions in mind, we formulate the equations governing the electrostatic field. The electrostatic potential, ϕ, satisfies

$$\nabla^2 \phi = 0, \tag{1}$$

$$\phi(aR(\theta), \theta, z') = 0 \qquad z' \in [0, L], \qquad \theta \in [0, 2\pi], \tag{2}$$

$$\phi(r', \theta, 0) = 0 \qquad r' \in [0, aR(\theta)], \qquad \theta \in [0, 2\pi], \tag{3}$$

$$\phi(r', \theta, u'(r', \theta)) = V \qquad r' \in [0, a], \qquad \theta \in [0, 2\pi], \tag{4}$$

where here $u'(r', \theta)$ is the displacement of the membrane from $z' = L$. The membrane is treated as a simple elastic membrane and hence the displacement is assumed to satisfy

$$T \nabla_\perp^2 u' = \frac{\epsilon_0}{2} |\nabla \phi|^2. \tag{5}$$

Here, T is the tension and ϵ_0 the permittivity of free space. The notation $\nabla_\perp$ indicates that derivatives are taken in the r' and θ directions only. We assume the membrane is held fixed along its circumference and impose

$$u'(aR(\theta), \theta) = L. \tag{6}$$

Next, we introduce dimensionless variables and rewrite our governing equations in dimensionless form. We define

$$\psi = \phi/V, \;\; u = u'/L, \;\; r = r'/a, \;\; z = z'/L \tag{7}$$

and substitute these in Equations (1–6). This yields

$$\epsilon^2 \nabla_\perp^2 \psi + \frac{\partial^2 \psi}{\partial z^2} = 0, \tag{8}$$

$$\psi(r, \theta, 0) = 0 \qquad r \in [0, R(\theta)], \qquad \theta \in [0, 2\pi], \tag{9}$$

$$\psi(R(\theta), \theta, z) = 0 \qquad z \in [0, 1], \qquad \theta \in [0, 2\pi], \tag{10}$$

$$\psi(r, \theta, u) = 1 \qquad r \in [0, R(\theta)], \qquad \theta \in [0, 2\pi], \tag{11}$$

$$\nabla_\perp^2 u = \lambda(\epsilon^2 |\nabla_\perp \psi|^2 + \psi_z^2), \tag{12}$$

$$u(R(\theta), \theta) = 1. \tag{13}$$

Here $\epsilon = L/a$ is an aspect ratio comparing device radius to gap size and $\lambda = \epsilon_0 V^2 a^2 / 2TL^3$ is a dimensionless number which characterizes the relative strengths of electrostatic and mechanical forces in the system.

3. A uniformly valid asymptotic theory

In this section we focus on the electrostatic problem, Equations (8–11), and derive a uniformly valid asymptotic approximation to the potential. We follow the approach we outlined in [13] for a circular membrane. We begin by making the small-aspect-ratio assumption, that is, we assume $\epsilon \ll 1$. If we simply let $\epsilon \to 0$, the partial differential equation in Equation (8) reduces to

$$\frac{\partial^2 \psi}{\partial z^2} = 0, \tag{14}$$

which is easily integrated to yield

$$\psi = \frac{z}{u}. \tag{15}$$

Note that this is the approximate electrostatic field used by most authors investigating electrostatically actuated MEMS. However, this solution is not valid near $r = R(\theta)$ as we cannot satisfy the condition that $\psi(R(\theta), \theta, z) = 0$. Hence, we take this solution as an outer solution in a boundary-layer theory and attempt to insert a boundary-layer at the walls by introducing the stretched variable

$$\eta = \frac{R(\theta) - r}{\epsilon}$$

into Equations (8–11). With this change of variables the problem in our inner region becomes

$$\frac{\partial^2\psi}{\partial\eta^2}-\frac{\epsilon}{R(\theta)-\epsilon\eta}\frac{\partial\psi}{\partial\eta}+\frac{\epsilon}{(R(\theta)-\epsilon\eta)^2}\left(R''\frac{\partial\psi}{\partial\eta}+2R'\frac{\partial^2\psi}{\partial\theta\eta^2}+\frac{R'^2}{\epsilon}\frac{\partial^2\psi}{\partial\eta^2}+\epsilon\frac{\partial^2\psi}{\partial\theta^2}\right)+\frac{\partial^2\psi}{\partial z^2}=0, \tag{16}$$

$$\psi(\eta,\theta,0)=0, \qquad \psi(0,\theta,z)=0, \qquad \psi(\eta,\theta,u(R(\theta)-\epsilon\eta,\theta))=1. \tag{17,18,19}$$

If we let $\epsilon\to 0$ here, we obtain

$$\frac{\partial^2\psi}{\partial\eta^2}+\frac{R'^2}{R^2}\frac{\partial^2\psi}{\partial\eta^2}+\frac{\partial^2\psi}{\partial z^2}=0, \tag{20}$$

$$\psi(0,\theta,z)=0, \qquad \psi(\eta,\theta,0)=0, \qquad \psi(\eta,\theta,1)=1. \tag{21,22,23}$$

We need one more condition to complete the specification of the inner problem. This comes from matching to our outer solution. We impose

$$\lim_{\eta\to\infty}\psi(\eta,\theta,z)=\lim_{r\to R(\theta)}\frac{z}{u(r,\theta)}=z. \tag{24}$$

The inner or boundary-layer problem defined by Equations (20–24) can now easily be solved. We find

$$\psi(\eta,z)=z+\frac{2}{\pi}\sum_{n=1}^{\infty}\frac{(-1)^n}{n}\exp\left(\frac{-n\pi\eta}{\sqrt{1+R'^2/R^2}}\right)\sin(n\pi z). \tag{25}$$

Finally, adding our outer approximation, Equation (15), to our inner approximation, Equation (25), and subtracting the common part, we obtain the following leading-order uniformly valid asymptotic approximation to the electrostatic field

$$\psi_{\text{uniform}}(\eta,z)=\frac{z}{u(r,\theta)}+\frac{2}{\pi}\sum_{n=1}^{\infty}\frac{(-1)^n}{n}\exp\left(-n\pi\left(\frac{R(\theta)-r}{\epsilon\sqrt{1+R'^2/R^2}}\right)\right)\sin(n\pi z). \tag{26}$$

Note that the first term in the uniform approximation is identical to the standard approximation made by most authors. The second term accounts for fringing fields near the boundary.

3.1. The electrostatic force

In order to compute the force on the membrane, we need to compute the quantity

$$\epsilon^2|\nabla_\perp\psi|^2+\psi_z^2, \tag{27}$$

evaluated at $z=u(r,\theta)$ as appears in Equation (12). This can be rewritten as

$$\epsilon^2\left(\psi_r^2+\frac{1}{r^2}\psi_\theta^2\right)+\psi_z^2. \tag{28}$$

Using our uniformly valid approximation, (27), to evaluate the force, we compute each of these terms:

$$\begin{aligned}\psi_r^2|_{z=u}=\frac{u_r^2}{u^2}&-\frac{4u_r}{\epsilon u\sqrt{1+R'^2/R^2}}\sum_{n=1}^{\infty}(-1)^n\exp\left(-n\pi\left(\frac{R(\theta)-r}{\epsilon\sqrt{1+R'^2/R^2}}\right)\right)\sin(n\pi u)\\&+\frac{4}{\epsilon^2\sqrt{1+R'^2/R^2}}\left(\sum_{n=1}^{\infty}(-1)^n\exp\left(-n\pi\left(\frac{R(\theta)-r}{\epsilon\sqrt{1+R'^2/R^2}}\right)\right)\sin(n\pi u)\right)^2,\end{aligned} \tag{29}$$

$$\psi_z^2|_{z=u} = \frac{1}{u^2} - \frac{4}{u}\sum_{n=1}^{\infty}(-1)^n \exp\left(-n\pi\left(\frac{R(\theta)-r}{\epsilon\sqrt{1+R'^2/R^2}}\right)\right)\cos(n\pi u)$$
$$+4\left(\sum_{n=1}^{\infty}(-1)^n \exp\left(-n\pi\left(\frac{R(\theta)-r}{\epsilon\sqrt{1+R'^2/R^2}}\right)\right)\cos(n\pi u)\right)^2, \tag{30}$$

$$\frac{1}{r^2}\psi_\theta^2|_{z=u} = \frac{1}{r^2}\frac{u_\theta^2}{u^2} + \frac{4u_\theta}{\epsilon r^2 u}\frac{\mathrm{d}}{\mathrm{d}\theta}\left(\frac{R(\theta)-r}{\sqrt{1+R'^2/R^2}}\right)\sum_{n=1}^{\infty}(-1)^n \exp\left(-n\pi\left(\frac{R(\theta)-r}{\epsilon\sqrt{1+R'^2/R^2}}\right)\right)\sin(n\pi u)$$
$$+\frac{4}{\epsilon r^2}\left(\frac{\mathrm{d}}{\mathrm{d}\theta}\left(\frac{R(\theta)-r}{\sqrt{1+R'^2/R^2}}\right)\sum_{n=1}^{\infty}(-1)^n \exp\left(-n\pi\left(\frac{R(\theta)-r}{\epsilon\sqrt{1+R'^2/R^2}}\right)\right)\sin(n\pi u)\right)^2. \tag{31}$$

3.2. The standard and corrected models

It is useful to state and compare the elastic problems resulting from the standard electrostatic approximation and the uniform approximation. When only the outer solution for ψ is used, the resulting elastic problem is

$$\nabla_\perp^2 u = \frac{\lambda}{u^2} \tag{32}$$

with $u=1$ on the boundary of the membrane. Equation (32) is the model studied by most investigators of electrostatic MEMS. As noted above, the elastic theory might be extended to deal with beams or plates, resulting in a change to the left-hand side of Equation (32), but the electrostatic force remains unchanged. Equation (32) generalized to plates may be found in [9]. If the uniformly valid approximation for the electrostatic field is used, the resulting elastic problem is

$$\nabla_\perp^2 u = \frac{\lambda}{u^2} + \lambda F(u, u_r, u_\theta, \eta, \epsilon), \tag{33}$$

again with $u=1$ on the boundary. Here the function F represents the appropriate sum of the terms computed in the previous subsection.

The obvious reason for studying (32) in place of (33) is simplicity and, as we shall see in the next section, this simplicity has allowed for much progress in the analysis of (32). In turn, this has allowed a deeper understanding of the pull-in instability and related MEMS-design issues. However, the question remains: how do the correction terms in Equation (33) change the solution set of Equation (32)? Or more physically: what is the effect of aspect ratio on device behavior?

Researchers focus on Equation (32) for another reason: one simply does not expect the effect of the neglected terms to be significant. After all, these terms come into play near the boundary, and most of the action in the deflection takes place far from the boundary! But while this argument is true for the electric field, it is false for the electrostatic force. A close examination of F reveals that there are terms that arise when using the uniformly valid approximation to the electric field to compute the electrostatic force that act everywhere, not just at the boundary. Following this line of thought, we propose a "corner-corrected theory" that neglects terms that only act in the boundary layer, yet includes terms that act throughout

the domain. We obtain this corner-corrected model by examining each of the terms in Equation (33) and ignoring those that are exponentially small away from the boundary. We retain all other terms. Our corner-corrected model is

$$\nabla_{\perp}^2 u = \frac{\lambda(1+\epsilon^2|\nabla u|^2)}{u^2} \tag{34}$$

with $u=1$ on the boundary. Note that the new terms included in Equation (34) are most significant when the gradient of u becomes large, *i.e.*, near corners. Hence the nomenclature "corner-corrected theory." We will investigate the effect of including these terms in Section 5.

4. Elements of the standard theory

As with many semi-linear elliptic problems, Equation (32) has been found to have a rich and surprising solution set. Lack of uniqueness [9, 13], symmetry-breaking in nonsimply connected domains [14], and the existence of infinitely many solutions for a single value of λ [13] have all been shown to be present. Much of this behavior stems from the simple fact that no matter what the choice of domain, no solution exists to Equation (32) when λ is sufficiently large. This result is embodied in the following theorem:

Theorem 1. *Let Ω be a bounded domain in $\mathbb{R}^2$ with smooth boundary $\partial\Omega$. Consider Equation* (32) *with Dirichlet boundary condition $u=1$. Then, there exists a λ^* such that no solution u exists for any $\lambda>\lambda^*$. Further, λ^* satisfies $\frac{4}{27}\mu_1 \le \lambda^* \le \frac{4}{27}\kappa_1$ where κ_1 is the first eigenvalue of the Laplacian over the domain and μ_1 is the first eigenvalue of the Laplacian over a suitably enlarged domain.*

A proof of this theorem may be found in [9]. As indicated in the introduction this theorem is intimately related to the well-known "pull-in" instability in MEMS. The nonexistence of solutions for Equation (32) is typically interpreted as the occurrence of pull-in. The value of λ^* provides the pull-in voltage, which is an important quantity in MEMS-device design. In the dynamic, damped version of the problem, which models the actual time-dependent behavior of many MEMS devices, it is observed that, for small values of λ, the membrane approaches a smooth steady-state deflection. When λ exceeds a critical value, the membrane collapses onto a nearby membrane — the displacement u tends to 0 at at least one point. The transition point dividing these two behaviors is λ^*. This provides another motivation for understanding λ^* as a function of domain shape.

In addition to the general results above, the solution set for (32) has been completely characterized for some special domains. In one-dimension, or in the case of an infinite strip in $\mathbb{R}^2$, the problem may be reduced to

$$\frac{\mathrm{d}^2 u}{\mathrm{d}x^2} = \frac{\lambda}{(1+u)^2} \quad \text{for } -1<x<1, \tag{35}$$

$$u(-1)=u(1)=0. \tag{36}$$

Note, for convenience in visualizing the bifurcation diagram, the change of variables $u \to 1+u$ has been introduced. In this case, a closed-form solution for u may be constructed [9]. It is easily shown that there are precisely two solutions when $0 \le \lambda < \lambda^*$, one solution when $\lambda=\lambda^*$, and no solutions for $\lambda>\lambda^*$. This leads to a bifurcation diagram with a single *fold*. That is, when λ is plotted against a measure of the solution, the resulting curve appears as in Figure 3. Also note that, if we step out along the solution curve, starting at $\lambda=0$, $\|u\|_\infty=0$,

we end up at $\lambda = 0$, $\|u\|_\infty = 1$. This implies that at the "end" of the solution curve we have reached a *singular solution* since u must necessarily equal -1 at some point and from Equation (35) the solution cannot be smooth. Since this solution is a limit of regular or smooth solutions, it is called a *limiting singular solution*. This nomenclature was introduced by Joseph and Lundgren [15].

In the case where the domain is a disk in $\mathbb{R}^2$, Equation (32) may be reduced to an ODE, again with a change of variables for convenience,

$$\frac{d^2u}{dr^2} + \frac{1}{r}\frac{du}{dr} = \frac{\lambda}{(1+u)^2} \quad \text{for } 0 < r < 1, \tag{37}$$

$$\frac{du}{dr}(0) = 0 \qquad u(1) = 0. \tag{38}$$

The fact that derivatives in the angular direction may be ignored follows from a result of Gidas, Ni, and Nirenberg. In particular, for the disk, the results of Gidas, Ni, and Nirenberg imply that all solutions are purely radial. Hence, it is sufficient to study (37). Equations (37–38) were studied in [13, 16, 17]. While a closed-form solution does not exist, similarity methods may be used to reduce the analysis of (37–38) to the analysis of an autonomous second-order initial-value problem. Phase-plane techniques may be used to completely characterize the solution set. In this case, for any integer n, there is at least one value of λ, say λ_n, for which precisely n solutions to Equations (37–38) exist. This leads to a bifurcation diagram with multiple folds as shown in Figure 4. Note that the sequence $\{\lambda_n\}_{n=1}^{\infty}$ converges to 4/9. That is, the limiting singular solution for the disk occurs at $\lambda = 4/9$.

The results for the strip and disk leave open the question of the multiplicity of solutions for the standard theory on a general domain. Which is more typical, the strip or the disk? To address this question we turn to numerical simulations of (32) in 2D, again with $u \to 1 + u$:

$$\nabla_\perp^2 u = \frac{\lambda}{(1+u)^2} \quad \text{for } x \in \Omega, \tag{39}$$

$$u = 0 \quad \text{on } \partial\Omega. \tag{40}$$

For this study we consider cases where Ω is a rectangle or an ellipse. In both of these domains we exploit symmetry to solve (39) on a quarter domain in the first quadrant and

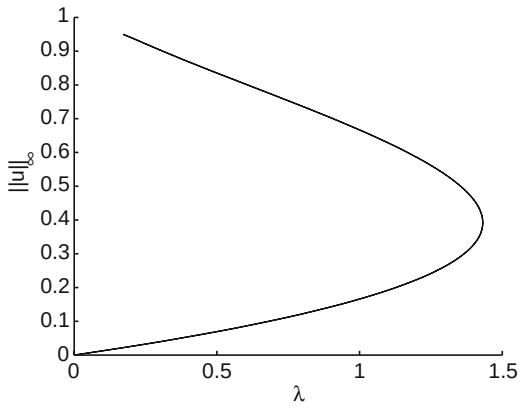

Figure 3. Numerically obtained bifurcation diagram for a strip-shaped system. Analytically it can be shown that the curve continues all the way to the point $(0, 1)$.

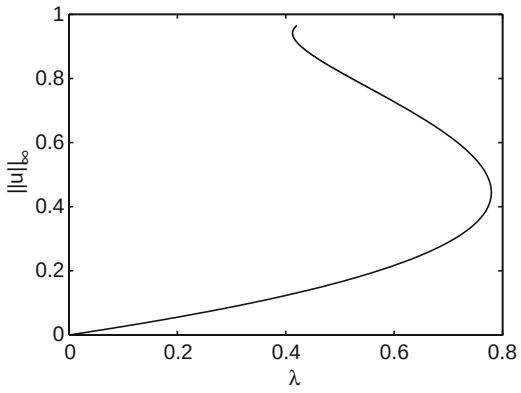

Figure 4. Bifurcation diagram for a disk-shaped system. The true curve continues folding infinitely many times as the point $(4/9, 1)$ is approached.

replace (40) with a homogeneous Neumann condition on the symmetry boundaries. For all cases we employ pseudospectral (spectral collocation) discretizations [18, 19] for the spatial Laplacian and pseudo-arc length continuation [20] to track the nonlinear eigenvalue problem.

When Ω is the quarter-rectangle $[0, a] \times [0, 1]$, we start with a tensor-product grid of Chebyshev-polynomial extreme points

$$(x_i, y_j) = \left(\frac{a}{2}\left[1 - \cos\left(\frac{i\pi}{N_x}\right)\right], \frac{1}{2}\left[1 - \cos\left(\frac{j\pi}{N_y}\right)\right] \right), \quad i = 0, \ldots, N_x, \quad j = 0, \ldots, N_y.$$

The unknown u is represented by an $(N_x + 1) \times (N_y + 1)$ matrix U of values on this grid. We can then define differentiation matrices that operate on each row (from the right) or each column (from the left) of U to compute y- or x-derivatives, respectively. These matrices incorporate the boundary conditions implicitly. For instance, let D be the standard Chebyshev differentiation matrix on $N_x + 1$ nodes (with a scale factor of $2/a$). We define

$$D_x^{(2)} = D_{1:N_x, 2:N_x+1} \, D_{2:N_x+1, 1:N_x}$$

as the discrete analog of $\partial^2/\partial x^2$, where the subscripts show row and column ranges extracted from D. The "outer" ranges enforce the Dirichlet condition on the last row of U — we assume those values are zero and do not compute derivatives there — and the "inner" ranges similarly enforce the Neumann condition on the first row of $\partial U/\partial x$. With a similar one-dimensional construction for $D_y^{(2)}$, the discrete Laplacian can be applied to U as $D_x^{(2)} U D_y^{(2)T}$. Finally, through Kronecker products we can equate this expression to $L\,\mathrm{vec}(U)$, where $\mathrm{vec}(U)$ is the vector resulting from stacking the columns of (nontrivial entries of) U, and L is a $N_x N_y \times N_x N_y$ matrix with a particular block-sparsity pattern. For more details on these matters, see *e.g.* [19].

When Ω is a quarter of the ellipse with semiaxes a and 1, we use generalized polar coordinates $x = ar\cos\theta$, $y = r\sin\theta$. One finds that

$$\begin{aligned} \nabla_\perp^2 = &\left(\frac{c^2}{a^2} + s^2\right)\partial_{rr} + \frac{\sin 2\theta}{r}\left(1 - \frac{1}{a^2}\right)\partial_{r\theta} + \left(\frac{s^2}{a^2} + c^2\right)\partial_{\theta\theta} \\ &+ \frac{1}{r}\left(\frac{s^2}{a^2} + c^2\right)\partial_r + \frac{\sin 2\theta}{r^2}\left(\frac{1}{a^2} - 1\right)\partial_\theta, \end{aligned} \tag{41}$$

where $c = \cos\theta$, $s = \sin\theta$. We now have a tensor product $(r, \theta) \in [0, a] \times [0, \pi/2]$ and can proceed much as in the rectangle. However, in θ we choose to extend the data symmetrically to a periodic function and differentiate using trigonometric interpolation (*i.e.*, Fourier pseudospectral), allowing us to use an equispaced grid in that direction. In r we have a Dirichlet condition at $r = a$ and an artificial singularity at $r = 0$ caused by the polar grid. Although one often simply avoids placing a grid point at this pole [18], in this case the origin is where $|u|$ is maximized and we have found it important to include this point. We assume that by symmetry $u_x = u_y = 0$ at the origin, which implies

$$u_r = 0, \qquad \frac{u_\theta}{r} = 0.$$

Using l'Hôpital's rule, we have

$$\frac{u_{r\theta}}{r} = u_{rr\theta}, \qquad \frac{u_{\theta\theta}}{r^2} = \frac{1}{2}u_{rr\theta\theta}, \qquad \frac{u_\theta}{r^2} = \frac{1}{2}u_{rr\theta},$$

which, when substituted in (41), leads to

$$\nabla_{\perp}^2|_{r=0} = \left(\frac{1}{a^2}+1\right)\partial_{rr} + \frac{1}{2}\left(\cos^2\theta + \frac{\sin^2\theta}{a^2}\right)\partial_{rr\theta\theta} + \frac{\sin 2\theta}{2}\left(1-\frac{1}{a^2}\right)\partial_{rr\theta}. \tag{42}$$

At a practical level, one forms a differentiation matrix based on (41), removes all but one of the columns and rows corresponding to $r=0$, and substitutes (42) for the remaining row.

We observe that, as $\|u\|_\infty \to 1$, the solution of (39) changes rapidly in the vicinity of the origin as a singularity apparently develops. Hence the clustering of Chebyshev nodes near the ends of an interval fortuitously provides us with high resolution where it is needed. However, it also wastes resolution near other boundaries. To improve on this we introduce the change of variable

$$x(\xi) = \frac{1-e^{-c\xi}}{1-e^{-c}}, \tag{43}$$

which maps [0, 1] to itself for real c and is the identity map if $c=0$. For $c>0$ an equispaced grid in ξ becomes skewed toward zero in x. Hence on the rectangle we use (43) on both x and y to concentrate more points near the origin, and in the ellipse we apply it to r for the same effect. By the chain rule this has the effect of premultiplying primitive one-dimensional differentiation matrices by a diagonal matrix.

Once the discretization is defined, (39) becomes the discrete system $F(u,\lambda)=0$, where now u represents a vector in $\mathbb{R}^m$ and F maps $\mathbb{R}^{m+1}$ to $\mathbb{R}^m$. This equation describes a curve in (u,λ)-space that we want to trace. The combination $u=0$, $\lambda=0$ is always a solution and thus will be considered our starting point.

In order to accommodate turning points on the curve, we introduce a pseudo-arclength scalar parameter s. Given previous values (u_{k-1},λ_{k-1}) and (u_k,λ_k) on the curve $F(u,\lambda)=0$ at $s=s_0$ and $s=s_1$, and given an increment δ_k, we find the next point on the curve as the solution of

$$F(u,\lambda)=0, \qquad (u_k-u_{k-1})^T(u-u_k)+(\lambda_k-\lambda_{k-1})(\lambda-\lambda_k)=\delta_k^2. \tag{44a,b}$$

(To get the continuation started at (u_1,λ_1), we use the definitions $u_{-1}=0$ and $\lambda_{-1}=-1$.) For small increments, Equation (44b) is a good approximation to the arclength condition $\|du/ds\|^2+(d\lambda/ds)^2=1$ and is linear in the unknowns. Equation (44) is a square system that can be solved by a Newton or quasi-Newton method. In our calculations we require solution of this system to a residual tolerance of 10^{-6}. We have found it useful to adapt the stepsize δ_k based on the local curvature and the contraction rate of the Newton steps, as described in [21]. Typically the method takes large steps initially but very small steps as $\|u\|_\infty \to 1$. More robust continuation methods are also described in [21]; we have also tried an Euler–Newton strategy, without significantly better results.

The algorithms were implemented and run entirely in MATLAB. As a test of our method, we recreated the results of Figure 4. In Figure 5 we show the curve computed as before and compare to four simulations done in a quarter-disk, using (r,θ) grids of 32×32 and 40×40 with grid skewing parameter $c=1,2$ in (43). The entire calculation shown took about five minutes on a PC workstation. The agreement is excellent at least for $\|u\|_\infty \le 0{\cdot}98$, and all of the simulations clearly show a second fold.

Figures 6 and 7 show our best results for rectangles and ellipses of aspect ratios 1, 2, 4, and 8. In each case the simulation used about 1500 unknowns and skew parameter $c=2$. We feel the evidence strongly suggests that multiply-folded bifurcation curves are generic in two dimensions. Note that this seems to hold even for an 8-by-1 rectangle that is beginning to approximate the idealized strip.

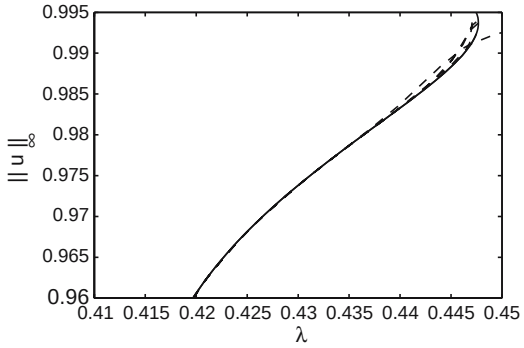

Figure 5. Comparison of full 2D simulations of (39) – (40) with the initial-value problem results shown in Figure 4 (solid curve). Dashed curves show 32×32 grids and 40×40 grids using different grid skewing parameters. Differences are visible only as $\|u\|_\infty$ approaches 1.

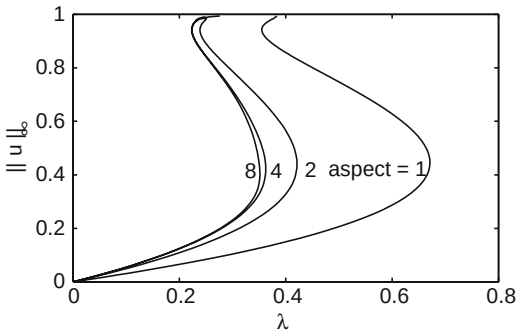

Figure 6. Bifurcation diagrams for rectangular systems of four different aspect ratios.

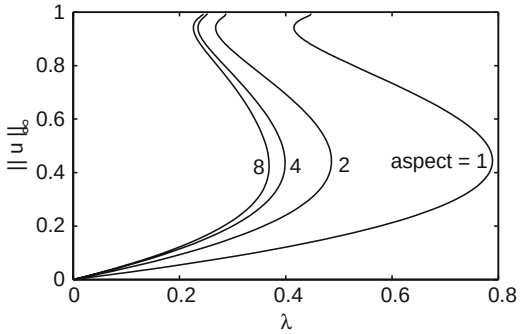

Figure 7. Bifurcation diagrams for elliptical systems of four different aspect ratios.

5. The effect of correction terms

In this section we take up the question of the effect of the correction terms introduced in our asymptotic theory on the solution set of the standard model. In particular, we consider how the solution set for Equation (32) differs from that of Equation (33), and explore the dependence on the parameter ϵ. We begin by noting that perhaps the most essential feature of the standard model, Equation (32), remains basically unchanged — the pull-in phenomenon persists. This is embodied in the following theorem, which is an extension of Theorem 1 to Equation (33).

Theorem 2. *Let Ω be a bounded domain in $\mathbb{R}^2$ with smooth boundary $\partial\Omega$. Consider Equation (33) with Dirichlet boundary condition $u = 1$. Then, there exists a λ^* such that no solution u exists for any $\lambda > \lambda^*$. Further, λ^* satisfies $\frac{4}{27}\mu_1 \leq \lambda^* \leq \frac{4}{27}\kappa_1$ where κ_1 is the first eigenvalue of the Laplacian over the domain and μ_1 is the first eigenvalue of the Laplacian over a suitably enlarged domain.*

Sketch of Proof for Theorem 2. The methods used to prove Theorem 1 are easily extended to prove Theorem 2. We skip the details and simply recall the basic ideas. The non-existence result, *i.e.*, establishing the fact that λ^* exists follows from an application of the Fredholm Alternative Theorem to Equation (33) after the first eigenfunction of the Laplace operator

has been subtracted from both sides. An interesting observation buried in the details of the proof is that the upper bound on λ^* decreased with increasing ϵ. The existence result follows by applying the method of upper and lower solutions. A constant serves as an upper solution and a multiple of an eigenfunction of the Laplace operator on an enlarged domain serves as a lower solution. The lower bound on λ^* follows from construction of the lower solution.

To investigate the effect of the correction terms more carefully, we restrict our attention to the case where the domain is a circular disk. In this case, our corrected theory becomes

$$\frac{d^2u}{dr^2}+\frac{1}{r}\frac{du}{dr}=\frac{\lambda}{(1+u)^2}+\frac{\epsilon^2\lambda}{(1+u)^2}\left(\frac{du}{dr}\right)^2 \quad \text{for } 0<r<1, \tag{45}$$

$$\frac{du}{dr}(0)=0 \quad u(1)=0. \tag{46}$$

The symmetry present and exploited when $\epsilon=0$ disappears for $\epsilon>0$. We wish to inquire as to how the destruction of the symmetry effects the bifurcation diagram of the standard theory. We turn to numerical solutions and visualize the effect of choosing $\epsilon>0$ by plotting the *meander* for the boundary-value problem. First, it is convenient to make the change of variables $1+u\to u$ resulting in

$$\frac{d^2u}{dr^2}+\frac{1}{r}\frac{du}{dr}=\frac{\lambda}{u^2}+\frac{\epsilon^2\lambda}{u^2}\left(\frac{du}{dr}\right)^2 \quad \text{for } 0<r<1, \tag{47}$$

$$\frac{du}{dr}(0)=0 \qquad u(1)=1. \tag{48}$$

Next, we integrate the ODE from $r=0$ to $r=1$, choosing all possible values of $u(0)$. We then plot the curve defined by $(u(1),u'(1))$ and parameterized by $u(0)$. Each time this curve intersects the line $u(1)=1$, we have a solution to the boundary-value problem. Several meanders for various values of ϵ are shown in Figure 8. When $\epsilon=0$, the meander is a spiral. As λ is varied this spiral passes from the left to the right of the line $u(1)=1$. This accounts for the increasing number of solutions to the boundary-value problem as λ is increased to one, the infinity of solutions at $\lambda=4/9$, the decreasing number of solutions for $\lambda>4/9$, and finally the disappearance of all solutions when $\lambda>\lambda^*$, or equivalently when the meander has moved to

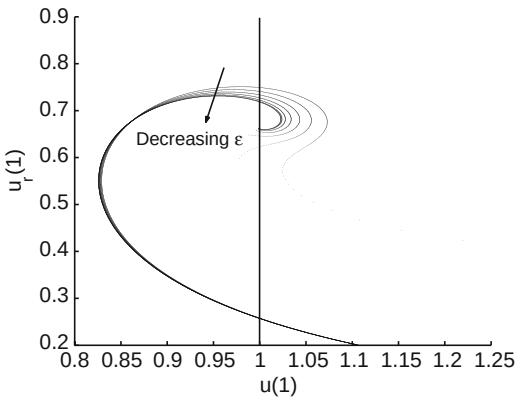

Figure 8. The meander for the corner corrected disk theory for various values of ϵ. Note the "unwinding" of the meander and the fact that when $\epsilon=0$, the meander is a spiral.

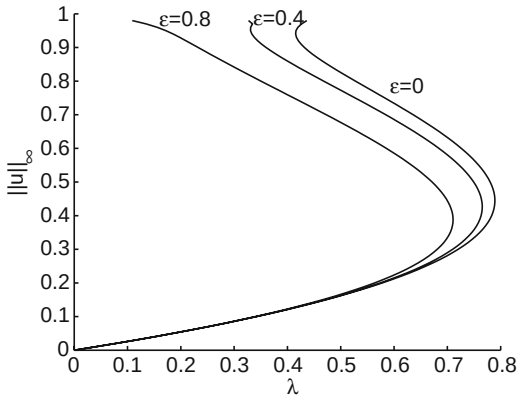

Figure 9. The bifurcation diagram for the corrected theory for various values of ϵ.

the right of $u(1)=1$. When ϵ is greater than zero, the meander "unwinds." The entire meander still moves to the right as λ is increased, but now the maximum number of intersections with the line $u(1)=1$ is always finite. Hence, the bifurcation diagram for $\epsilon > 0$ has a finite number of folds. The unwinding of the meander increases with ϵ and hence the number of folds decreases with increasing ϵ.

Further understanding of the behavior of the solutions of Equations (45–46) may be obtained by looking at the bifurcation diagram directly. To construct the bifurcation diagram we implement a simple continuation method for the boundary-value problem, Equations (45–46). The results for illustrative values of ϵ appear in Figure 9. Notice that, as ϵ is increased, the number of folds is decreased, as was expected from our look at various meanders for the system. Moreover, the position of the first fold point moves down and to the left.

6. Conclusions

We began with the goal of understanding the limitations of the standard model of electrostatically actuated MEMS devices. We recognized that one of the biggest approximations typically made by researchers in this area involves the electric field. In particular, a parallel-plate-like approximation which ignores fringing fields and field intensification near corners is standard in the MEMS community. To understand how effects ignored by this approximation might change the solution of a model of an electrostatic-elastic system, we constructed a mathematical model of a drum-shaped idealized MEMS device. Our system consists of an elastic membrane held at potential V capping a rigid drum held at zero potential. Our model included the equations for the electric field in the drum and for the elastic deflection of the membrane. Assuming a small but nonzero aspect ratio, we developed an asymptotic approximation for the electric field in the drum. In turn, this yielded an approximation for the electric force on our membrane. We compared our corrected model with the standard model and suggested a new "corner-corrected" theory. In order to explore the corner-corrected theory we needed to flesh out our understanding of the standard model. After reviewing the basic theory for the standard model on a strip and a disk, we used spectral numerical discretizations on rectangles and ellipses to provide strong evidence that the disk is typical — all domains exhibited a bifurcation diagram with multiple folds. Next, we returned to the corner-corrected model. We noted that the most important features of the standard model are still present in the corner-corrected model. These features are embedded in Theorem 2. In physical terms Theorem 2 establishes the existence of the pull-in instability in the corner-corrected model. We then focused on the corner-corrected model on a disk-shaped domain. This allowed a direct comparison with the most fully understood realization of the standard model. By examining the meander for the relevant boundary-value problem, we found that the correction terms we propose lead to an "unwinding" of the meander and consequently a change in the multiplicity of solution as a function of ϵ. Finally, we examined the bifurcation diagram for the corner-corrected theory directly. We note both the reduction in the multiplicity of solutions and the shift in the pull-in voltage as a function of ϵ.

Perhaps the most important implication of this work for MEMS device design concerns the shift in the pull-in voltage as a function of ϵ, the device aspect ratio. When attempting to design a MEMS device with the greatest range of motion possible, one wishes to operate right up to the pull-in voltage. Good estimates of the pull-in voltage lead to higher-performance designs. Here we have seen that it is important to correct for the aspect ratio when computing the pull-in voltage.

Acknowledgements

J.A.P. thanks the National Science Foundation #0305234 and the University of Delaware Research Foundation. T.A.D. thanks the National Science Foundation (DMS-0104229) and the Delaware students of MATH 612 in fall 2003 whose impressive efforts on the rectangle simulation helped confirm the results given here.

References

1. J. Crowley, *Fundamentals of Applied Electrostatics*. San Jose: Laplacian Press (1986) 272 pp.
2. H.C. Nathanson, W.E. Newell and R.A. Wickstrom, The resonant gate transistor. *IEEE Trans. on Electron Devices* 14 (1967) 117–133.
3. M. Bao and W. Wang, Future of microelectromechanical systems (MEMS). *Sensors and Actuators A* 56 (1996) 135–141.
4. H. Camon, F. Larnaudie, F. Rivoirard and B. Jammes, Analytical simulation of a 1D single crystal electrostatic micromirror. In: *Proceedings of Modeling and Simulation of Microsystems* (1999).
5. P.B. Chu and K.S.J. Pister, Analysis of closed-loop control of parallel-plate electrostatic microgrippers. In: *Proc. IEEE Int. Conf. Robotics and Automation* (1994) pp. 820–825.
6. H.A.C. Tilmans, M. Elwenspoek and J.H.J. Fluitman, Micro resonant force gauges. *Sensors and Actuators A* 30 (1992) 35–53.
7. M.J. Anderson, J.A. Hill, C.M. Fortunko, N.S. Dogan and R.D. Moore, Broadband electrostatic transducers: modeling and experiments. *J. Acoust. Soc. Am.* 97 (1995) 262–272.
8. M.T.A. Saif, B.E. Alaca and H. Sehitoglu, Analytical modeling of electrostatic membrane actuator micro pumps. *J. Microelectromech. Syst.* 8 (1999) 335–344.
9. J.A. Pelesko and D. Bernstein, *Modelling MEMS and NEMS*. Boca Raton, FL: Chapman and Hall/CRC (2003) 376 pp.
10. X.P. Zhao, E.M. Abdel-Rahman and A.H. Nayfeh, A reduced-order model for electrically actuated microplates. *J. Micromech. Microengng.* 14 (2004) 900–906.
11. O. Bochobza-Degabi, D. Elata and Y. Nemirovsky, An efficient DIPIE algorithm for CAD of electrostatically actuated MEMS devices. *J. Microelectromech. Syst.* 11 (2002) 612–620.
12. J.A. Pelesko and X.Y. Chen, Electrostatically deflected circular elastic membranes. *J. Electrostat.* 57 (2003) 1–12.
13. J.A. Pelesko, Electrostatic field approximations and implications for MEMS devices. In: *Proceedings of ESA 2001* (2001) pp. 126–137.
14. J.A. Pelesko, D.H. Bernstein and J. McCuan, Symmetry and symmetry breaking in electrostatic MEMS. In: *Proc. of MSM 2003* (2003) pp. 304–307.
15. D.D. Joseph and T.S. Lundgren, Quasilinear Dirichlet problems driven by positive sources. *Arch. Rational Mech. Anal.* 49 (1973) 241–269.
16. G.I. Taylor, The coalescence of closely spaced drops when they are at different electric potentials. *Proc. R. Soc. London A* 306 (1968) 423–434.
17. R.C. Ackerberg, On a nonlinear differential equation of electrohydrodynamics. *Proc. R. Soc. London A* 312 (1969) 129–140.
18. B. Fornberg, *A Practical Guide to Pseudospectral Methods*. Cambridge: Cambridge University Press (1996) 242 pp.
19. L.N. Trefethen, *Spectral Methods in MATLAB*. Philadelphia: Society for Industrial and Applied Mathematics (2000) 184 pp.
20. J.S. McGough, Numerical continuation and the Gelfand problem. *Appl. Math. Comp.* 89 (1998) 225–239.
21. E.L. Allgower and K. Georg, *Introduction to Numerical Continuation Methods*. Philadelphia: Society for Industrial and Applied Mathematics (2003) 388 pp.